

Ground-state coherence versus orientation: Competing mechanisms for light-induced magnetic self-organization in cold atoms

G. Labeyrie,^{1,*} J. G. M. Walker², G. R. M. Robb², R. Kaiser¹, and T. Ackemann²

¹Université Côte d'Azur, CNRS, Institut de Physique de Nice, 06560 Valbonne, France

²SUPA and Department of Physics, University of Strathclyde, Glasgow G4 0NG, Scotland, United Kingdom



(Received 16 November 2021; accepted 20 January 2022; published 7 February 2022)

We investigate the interplay between two mechanisms for magnetic self-organization in a cloud of cold rubidium atoms subjected to a retroreflected laser beam. The transition between two different phases, one linked to a spontaneous spatial modulation of the $\Delta m = 2$ ground-state coherence and the other to that of the magnetic orientation (spin), can be induced by tuning either a weak transverse magnetic field or the laser intensity. We observe both first- and second-order transitions depending on the presence of the magnetic field. The experimental observations are successfully compared to extended numerical simulations based on a spin-1 model.

DOI: [10.1103/PhysRevA.105.023505](https://doi.org/10.1103/PhysRevA.105.023505)

I. INTRODUCTION

Cold and ultracold atoms are nowadays increasingly used in quantum simulator approaches [1,2] to study classical [3] and quantum magnetism [4,5]. These studies usually involve the trapping of atoms in externally applied optical potentials of increasing complexity and reconfigurability [6]. The interactions between particles can be boosted using strongly dipolar gases [7,8] and polar molecules [9,10], or Rydberg atoms [11,12].

Another approach is to use *light* to mediate the interactions between atoms. Indeed, under the action of a retroreflected laser beam, a sample of cold atoms can self-organize without the presence of any external spatially modulated optical potential. The spontaneously arising spatial order, which can be long-range, may concern either external degrees of freedom (density) [13–15] or internal ones, such as excited-state populations [16] or Zeeman populations and coherences in the ground state [17,18]. In the case of density self-organization, the retroreflected scheme bears some similarities with transversely pumped cavities schemes [19–21], with the difference that self-organization occurs by breaking two continuous symmetries (translation and rotation in the plane transverse to beam propagation) due to the absence of a preferred axis (as in cavities).

In a previous work [17], we observed several self-organized magnetic phases in an experiment using a large cloud of cold ⁸⁷Rb atoms. The transition between these phases was induced by tuning the direction and magnitude of a weak magnetic field. In particular, applying the magnetic field along the laser beam's propagation axis led to the transition from a square-symmetry antiferromagnetic (AFM) phase to a hexagonal-symmetry ferrimagnetic (FM) phase [18]. The observed behavior of the AFM phase versus the magnetic field

was in agreement with predictions of the antiferromagnetic Ising model [22,23]. It was shown that both these phases are based on the spontaneous spatial modulation of the atomic ground-state orientation, roughly similarly to early observations in hot sodium vapors using an effective spin-1/2 system [24,25] but with additional subtleties due to the more complex atomic structure [26].

In the present work, we investigate a more exotic phase whose existence relies on the spontaneous modulation of the $\Delta m = 2$ atomic ground-state coherence. The physics at work here involves a quadrupole component of the magnetization [27], instead of the dipole term corresponding to orientation. By essence, this phase cannot occur in spin-1/2 systems. Hereafter, it is termed the “ground-state coherence” (GSC) phase. In the following, we first briefly describe in Sec. II the experimental setup and detection scheme. Then, in Sec. III, the spin-1 theoretical model and associated numerical simulations used for comparison with experimental findings are briefly discussed. In Sec. IV we describe the main features characterizing the GSC phase and discuss the range of parameters where it can be observed. Finally, in Sec. V, we study the different ways to induce a transition between the GSC and AFM phases, and we discuss the nature of these transitions.

II. SHORT DESCRIPTION OF EXPERIMENT

The self-organization phenomena that we study are due to an optical feedback scheme based on diffractive coupling [28,29]. A laser beam passes through a cloud of cold atoms, which results in deformations of its wave front. The transmitted wave is fed back to the cloud by a mirror after free-space propagation (hence the “diffractive” coupling). The diffracted wave reacts on the cloud's susceptibility due to an optical nonlinearity, producing feedback. In such a closed-loop system, various types of spatially self-organized phases can emerge, depending on the nature of the nonlinearity [14,16,17,24,30,31].

*guillaume.labeyrie@inphyni.cnrs.fr

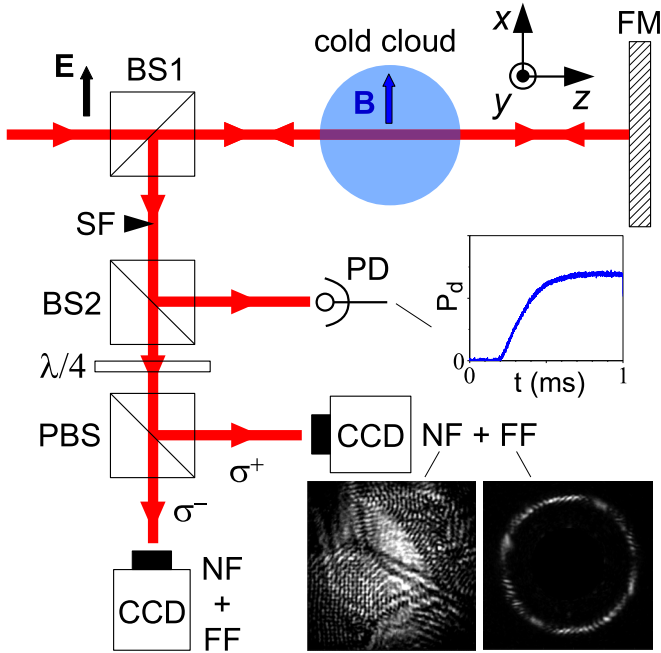


FIG. 1. Sketch of the experiment. A red-detuned laser beam passes through a large cold ^{87}Rb cloud. The beam is then retro-reflected, and its intensity distributions in near field and far field are recorded. Two orthogonal polarization channels are simultaneously analyzed. The temporal dynamics is recorded with a photodiode. See text for details.

The experiment proceeds as sketched in Fig. 1. A large cloud of cold ($T \approx 200 \mu\text{K}$) ^{87}Rb atoms is produced in a magneto-optical trap (MOT). The diameter of the cloud is around 13 mm (full width at half maximum) and its on-resonance optical density (OD) will be equal to 130 in the rest of the paper (except for the data of Fig. 8, where the OD is varied). This cloud is released from the MOT by switching off the trapping beams and the magnetic-field gradient and is then illuminated by a retroreflected laser beam of waist 2.2 mm ($1/e^2$ radius) and peak intensity I , detuned from the $F = 2 \rightarrow F' = 3$ transition of the D2 line by -12Γ ($\Gamma/2\pi = 6 \text{ MHz}$ is the natural width of the transition). Because of this relatively large detuning, the saturation parameter associated with the incident beam $s = \frac{I}{I_{\text{sat}}} \frac{1}{1+4(\delta/\Gamma)^2}$, where I_{sat} is the saturation intensity, will remain small throughout this paper ($5 \times 10^{-4} < s < 0.1$).

The laser beam also contains a few percent of “repumping” light to keep the atoms in the $F = 2$ ground state. The beam’s polarization is linear, aligned along the x axis in Fig. 1. The duration of the laser pulse is 1 ms. During the pulse duration, a weak magnetic field is applied to the cloud along the direction of the input laser beam’s polarization \mathbf{E} ($0 \leq B_x < 2.5 \text{ G}$, $B_y = B_z = 0$ except in Fig. 6). After detection of the various signals (see below), the MOT is turned on again and the whole cycle is repeated.

Part of the beam retroreflected by the feedback mirror (FM) is collected by a nonpolarizing beam splitter (BS1) and used for detection. A spatial filter (SF), which can be removed, blocks the “undiffracted” component of the light (or “zeroth order”) corresponding to the smooth incident Gaussian mode.

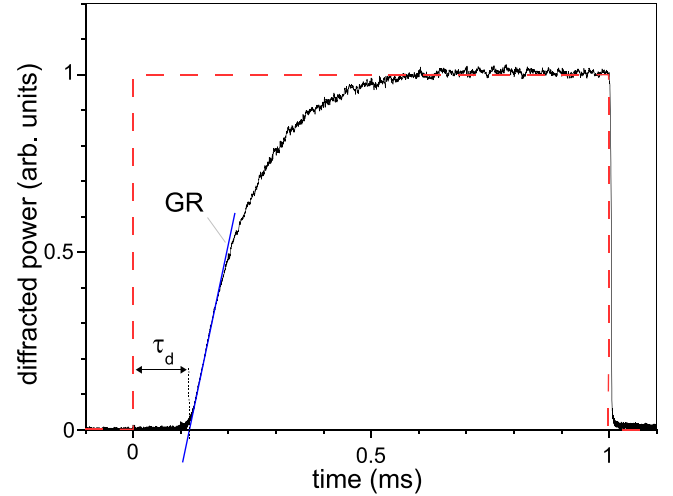


FIG. 2. Analysis of temporal dynamics (experimental). We show an example of the time dependence of the diffracted power. The intensity profile of the laser is shown as a dashed line. Using a linear fit of the initial growth, we extract the growth rate (GR) and the delay τ_d .

The “sideband” components of the light, which correspond to the light diffracted by the transverse spatial modulation of the cloud’s susceptibility, are unaffected by the spatial filter. A second nonpolarizing beam splitter (BS2) is used to send part of this light on a photodiode (PD) for time-resolved detection of the diffracted power P_d . The rest of the light is split into its circular polarization components by a quarter-wave plate ($\lambda/4$) + polarizing beam splitter (PBS) assembly. Alternatively, the $\lambda/4$ can be removed and the reflected beam’s polarization is separated into its linear components, parallel (lin // channel) and orthogonal (lin \perp channel) to the incident beam’s polarization. The transverse intensity distribution of the light in each polarization channel is detected both in near field (NF) and far field (FF) using CCD cameras. In NF (see Fig. 3), the imaged plane is chosen to visualize the “re-entrant” intensity distribution, i.e., the light that is fed back to the cloud. The FF, obtained in the focal plane of a lens (not shown in Fig. 1), corresponds to the angular distribution of the light (see Fig. 4). The diffracted sidebands show up as peaks on a circle whose radius is the transverse wave vector selected by the position of the feedback mirror [28].

Figure 2 shows an example of the dynamics of the diffracted power detected with the photomultiplier. By performing a linear fit of the initial rise, we can extract the growth rate (given by the slope of the fit) and the delay τ_d from laser turn-on (the dashed lines represent the intensity profile of the laser pulse). The area under the temporal profile is the diffracted energy E_d . Such a time-resolved detection is essential for the results presented in Sec. V.

III. THEORETICAL MODEL AND NUMERICAL SIMULATIONS

We briefly outline here the model used to describe our system. Details can be found in the supplementary material of Ref. [17]. Because of the low saturation used in the

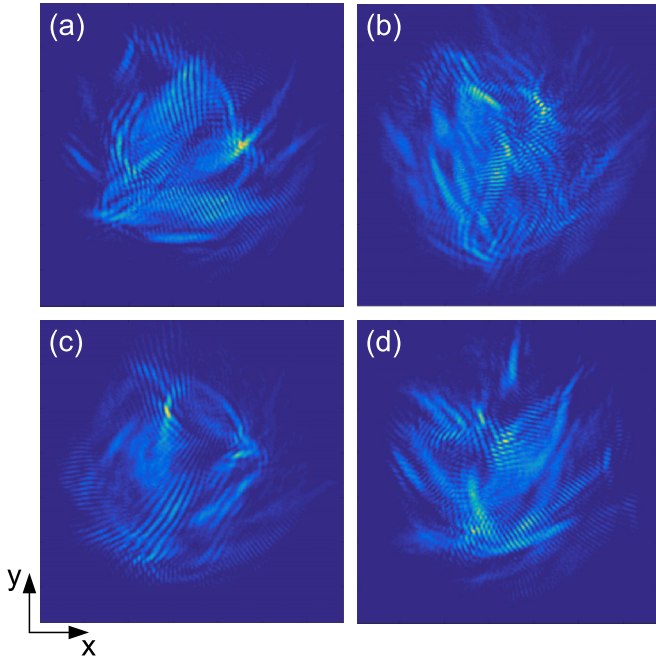


FIG. 3. Near-field distribution of the GSC phase in the lin \perp channel (experimental). The four panels illustrate shot-to-shot fluctuations of the observed patterns. The field of view is 5×5 mm. Parameters: $B_x = 1$ G, $I = 2$ mW/cm 2 .

experiments, we can safely neglect both optomechanical [14] and excited-state [16] pattern-forming mechanisms. The physics that we study here extends beyond that of a spin-1/2 system and ordinary Zeeman pumping [24]. However, it seems unrealistic to try modeling the full complexity of our experimental $F = 2 \rightarrow F' = 3$ transition. Thus, we settled for a $F = 1 \rightarrow F' = 2$ model transition that includes the necessary ingredients to explain most of our experimental observations.

Our observations are typically made at sufficiently low saturation such that all the relevant physics can be expressed in terms of ground-state quantities. Taking the quantization axis along the laser beam's propagation axis z , the relevant atomic variables are the orientation $w = \rho_{11} - \rho_{-1-1}$, the alignment $X = \rho_{11} + \rho_{-1-1} - 2\rho_{00}$, and the $\Delta m = 2$ ground-state coherence $\phi = 2\rho_{1-1} = u + iv$ (u and v are the real and imaginary parts of ϕ , respectively). Here, ρ_{ij} are the matrix elements of the ground-state Zeeman sublevels. In the description in terms of multipole moments of the magnetization [27], w corresponds to a dipole term, while X , u , and v are quadrupole terms. The connection between these atomic variables and the optical properties of the atomic cloud of thickness L is illustrated by the following expression describing the propagation of the circularly polarized components of the light field E_{\pm} through the cloud:

$$\frac{d}{dz}E_{\pm} = i\frac{\Phi_{\pm}}{L}\left[\left(1 \pm \frac{3}{4}w + \frac{1}{20}X\right)E_{\pm} + \frac{3}{20}(u \mp iv)E_{\mp}\right]. \quad (1)$$

Here, Φ_{\pm} are the linear phase shifts acquired by these fields upon traversing the cloud. Since the laser detuning is large, we

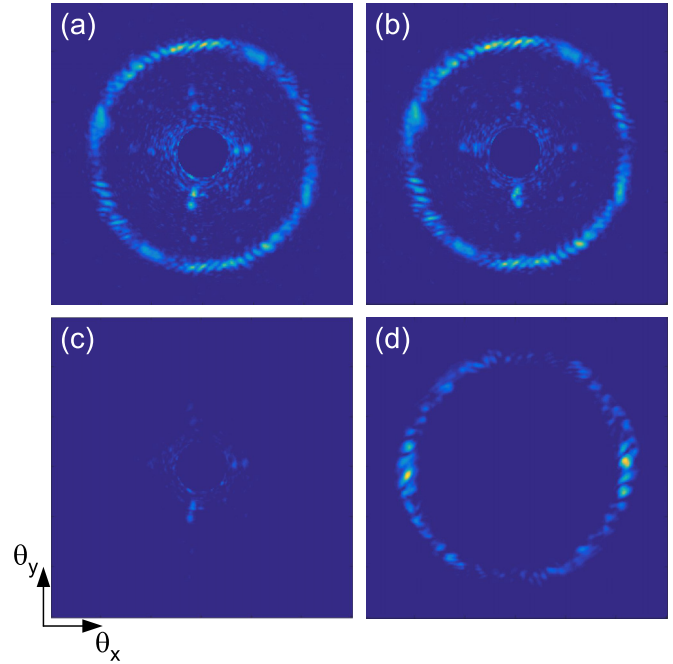


FIG. 4. Polarization distribution of the GSC phase (experimental). We show FF images (with the zeroth order blocked) recorded in each of the four polarization channels: (a) σ^+ , (b) σ^- , (c) lin $//$, and (d) lin \perp . The intensity scale is the same within each pair of orthogonal channels, but different for circular and linear channels. The field of view is 16 mrad \times 16 mrad. Parameters: $B_x = 1$ G, $I = 2$ mW/cm 2 .

neglect absorption and consider only the cloud's (real) index of refraction. The \pm and \mp signs in front of w and v show that the optical response due to these variables is polarization dependent, which can lead to a change of the polarization of the light field (polarization instability). On the contrary, the optical response due to the X and u variables is polarization preserving. Also, it is seen that both u and v allow for a cross-coupling between E_+ and E_- fields [17]. Indeed, these terms correspond to a “ Λ ” scheme where both fields address the same excited state.

The temporal evolution of the atomic variables is governed by a set of eight coupled equations involving pumping terms associated with the circular polarization components of the total light field. This total field is the sum of the forward-propagating field (incident beam) and the backward-propagating one (retroreflected one), for which diffraction is included to account for propagation between the cloud and the mirror and back (see Fig. 1). The interference between beams creates a longitudinal grating along z at the optical wavelength scale. However, since the response time of the atomic ground state is fairly large, the atoms travel several optical wavelengths during that time and the modulation averages out. Thus, we replace the pumping terms in the set of coupled equations by their spatial averages (along z). We numerically solve this set of coupled equations for the atomic parameters and light fields on a 128×128 grid and thus have access to both light intensity and atomic parameter distributions in the transverse plane (x , y). The simulations can be run using an

incident plane wave or a Gaussian beam, to better match the experimental observations (see Fig. 11B).

IV. OBSERVATION OF GSC PHASE

In this section, we describe the distinctive features of the GSC phase. As a general rule, this phase is observed when a magnetic field $B_x \neq 0$ is applied along the direction of the polarization of the incident laser beam [17]. Additional requirements on other parameters such as other B field components, laser intensity, or cloud OD are discussed in the following.

We show in Fig. 3 examples of near-field transverse light intensity distributions belonging to the GSC phase. These images correspond to single shots recorded in the $\text{lin} \perp$ channel, with the same parameters. As can be seen, the GSC phase is characterized by regions with relatively highly contrasted intensity structures separated by weakly contrasted regions. Unlike in the antiferromagnetic and ferrimagnetic phases [17, 18], there is usually no long-range order except on rare occasions. As a consequence, the FF image for the GSC phase usually consists of a ring with a fairly even intensity distribution (see Fig. 4). The structures typically observed in NF include stripes, zig-zags, checkerboards, and dots on a square lattice.

The polarization properties of the light are illustrated by the FF images shown in Fig. 4, where the zeroth order has been blocked. Figures 4(a) and 4(b) correspond to the two circular channels, and Figs. 4(c) and 4(d) correspond to the $\text{lin} //$ and $\text{lin} \perp$ channels, respectively. The intensity display is the same for Figs. 4(a) and 4(b) and for Figs. 4(c) and 4(d). Note that these four images were not recorded simultaneously (only two orthogonal channels can be recorded at the same time, see Fig. 1). As can be seen in these single-shot images, the FF intensity is fairly evenly distributed on the ring shape, which indicates a random orientation of the structures in the NF. In addition, the observation of Figs. 4(c) and 4(d) reveals that most of the diffracted light has a linear polarization, orthogonal to that of the incident beam. According to Eq. (1), this means that this phase is associated with a large spatial modulation of either w or v (or both). The measured ratio of the diffracted light power in the \perp and $//$ channels exceeds 100. As a comparison, this ratio is approximately 1 order of magnitude lower for the AFM phase ($B = 0$).

For comparison with the images in Fig. 3, we show in Fig. 5(a) the NF intensity distribution obtained for the GSC phase in the numerical simulation (incident plane wave, $\text{lin} \perp$ channel, $B_x = 0.76$ G, $I = 6.68$ mW/cm²). The NF typically exhibits stripelike structures of random orientation, separated by lines of defects. Figures 5(b), 5(c), and 5(d) show the corresponding distributions of the atomic parameters w , u , and v , respectively. As can be seen, the $\Delta m = 2$ Zeeman coherence and, in particular, its imaginary part v show a large spatial modulation which constitutes a signature of the GSC phase. The presence of this modulation in the GSC phase (and its much reduced value in the AFM phase) was experimentally demonstrated in Ref. [17]. We note in Fig. 5(b) that the orientation w also exhibits a sizable spatial modulation. This is not in itself surprising considering that w , u , and v are coupled variables in the equations describing the system. The exact

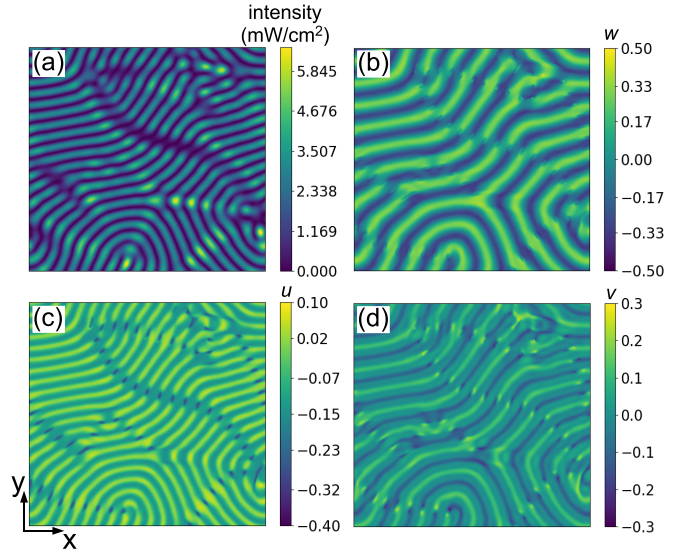


FIG. 5. Observation of the GSC phase (numerical). (a) NF intensity (mW/cm²) in $\text{lin} \perp$ channel, (b) w distribution, (c) u distribution, and (d) v distribution. The field of view is 1.8 mm \times 1.8 mm. Parameters: plane-wave input, $B_x = 0.76$ G, $I = 6.68$ mW/cm².

role played by the modulation of w in the establishment of the GSC phase is not understood at present, but that of ϕ is essential.

As pointed out before, the GSC phase is observed when a nonzero magnetic field is applied to the atomic cloud along the direction of input laser polarization. Increasing the magnetic field's components along the other axes (B_y or B_z) tends to destroy the coherence ϕ and hence the GSC phase, as illustrated in Fig. 6. In this figure, we plot the measured GSC phase's intensity threshold $I_{\text{th}}^{\text{GSC}}$ as the magnetic field's components are varied. In Fig. 6(a), both B_x and B_z are varied with $B_y = 0$. In Fig. 6(b), B_y and B_z are varied with $B_x = 0.71$ G. The curves in Fig. 6 are symmetric with respect to a change of sign of all B components. As can be seen, the threshold intensity increases as either B_y or B_z is increased. This is because the driving has to be increased to compensate for the decoherence induced by either B_y or B_z (or both). As B_x is increased, the (B_y , B_z) domain of observation of the GSC phase broadens. In three (B field) dimensions, the region of occurrence of the GSC phase thus has a "conical" shape whose axis is the B_x axis. Note that the tip of the cone corresponds to $B_x \neq 0$, as can be seen in Fig. 6(a): the GSC phase is not observed below a certain threshold value of B_x . Indeed, around zero magnetic field, the AFM phase relying on orientation is favored as can be expected by the large prefactor in front of w in Eq. (1). The coherence-based GSC phase can arise only when the orientation-based mechanism is reduced by the population mixing induced by $B_x \neq 0$ [17].

A striking feature of the GSC phase is the very low light level required for its formation. The lowest threshold intensity that we were able to measure is $I_{\text{th}}^{\text{GSC}} = 0.34$ mW/cm² (for OD = 100 and $\delta = -9\Gamma$). The corresponding peak saturation parameter for the incident beam is $s = 2.9 \times 10^{-4}$. Here, we have assumed even populations in all Zeeman substates of the ground state ($I_{\text{sat}} = 3.58$ mW/cm²). At this saturation level,

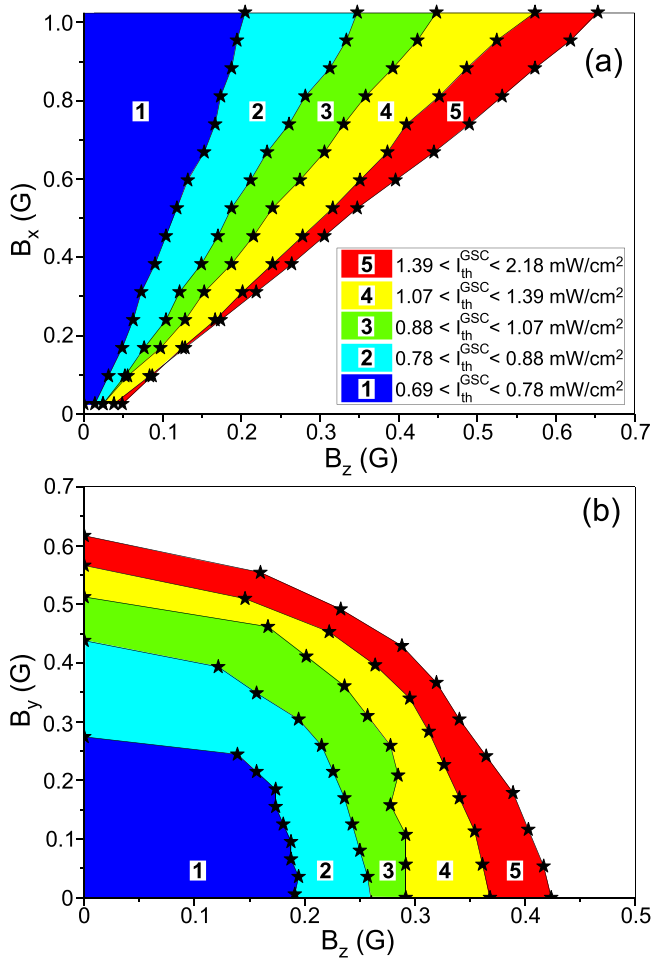


FIG. 6. Domain of observation of the GSC phase in the magnetic-field space (experimental). (a) GSC intensity threshold versus B_z and B_x ($B_y = 0$). (b) GSC intensity threshold versus B_z and B_y ($B_x = 0.71$ G).

only a few photons are exchanged between each atom and the laser field during a 1-ms-long laser pulse. As is discussed in the next section, a characteristic feature of the GSC phase is that it also presents an upper intensity threshold: the phase disappears above a certain laser intensity.

The formation of a self-organized phase requires the non-linear phase shift experienced by the incident wave to be above a certain threshold value, which in turn imposes a minimal value for the linear phase shift and thus the OD [14,16,17]. This threshold OD depends on the nature of the nonlinearity. It was already noted in Ref. [17] that the threshold OD for the GSC phase is larger than that for the AFM phase. This observation is confirmed and further illustrated in the next section.

V. TRANSITIONS BETWEEN GSC AND AFM PHASES

We concentrate in this section on the transition from the GSC phase to the nearby AFM phase and on the comparison of the nature of the bifurcations leading to these two phases. We use two different schemes to induce such a transition,

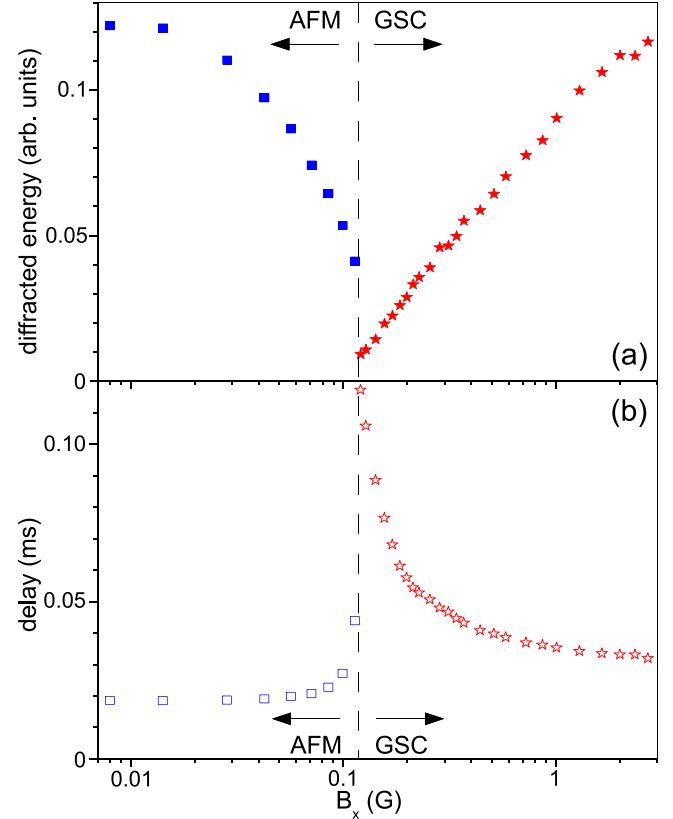


FIG. 7. Transition from AFM to GSC phase via B_x tuning (experimental). We plot in panel (a) the diffracted energy and (b) the delay as a function of B_x (in logarithmic scale). The squares and stars correspond to the AFM and GSC phases, respectively. The dashed line indicates the boundary between phases. The laser intensity is $I = 16.3 \text{ mW}/\text{cm}^2$.

either by tuning the transverse magnetic field B_x or the laser intensity I .

A. Magnetic-field-induced transition

A first way to observe the AFM-GSC transition is to start from the AFM phase, whose optimum occurs at $B_x = B_y = B_z = 0$, and to gradually increase B_x at constant laser intensity. As discussed before, above some critical B_x value the orientation-based mechanism associated with the AFM phase is no longer sustained because of the Zeeman substate mixing due to the transverse B -field, and the GSC phase takes over. The critical B_x depends on laser intensity: very roughly, the transition occurs when the Larmor frequency is of the order of the Rabi frequency.

This transition is experimentally observed in Fig. 7. We plot here the diffracted energy E_d [Fig. 7(a)] and the delay τ_d [Fig. 7(b)] for the two phases (squares correspond to AFM, stars to GSC) versus B_x in logarithmic scale. These quantities are extracted from time-resolved profiles such as shown in Fig. 2, detected in the \perp channel, which are averaged over 20 successive shots. In Fig. 7(a), for the AFM phase E_d drops when B_x is increased, as expected from the discussion above. At a critical field $B_x = 0.115$ G (dashed line), the transition to the GSC phase occurs. Above the critical field, for the

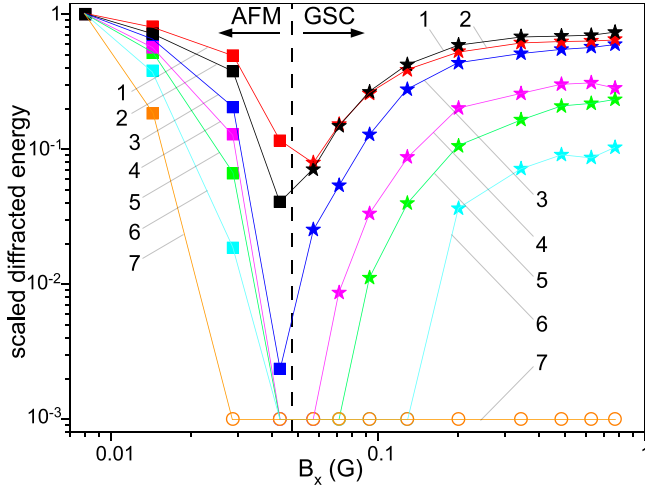


FIG. 8. Role of OD on AFM and GSC phases (experimental). We plot the scaled diffracted energy (see text) of the AFM (squares) and GSC (stars) phases versus B_x , for different values of OD: (1) OD = 110, (2) OD = 86, (3) OD = 57, (4) OD = 52, (5) OD = 41, (6) OD = 31, and (7) OD = 26. Note the double logarithmic scale. The laser intensity is $I = 3.6 \text{ mW/cm}^2$.

GSC phase E_d increases steadily with B_x . In Fig. 7(b), the delays for both phases are seen to diverge when approaching the transition. This is referred to as “critical slowing down,” a feature commonly observed near bifurcations [32]. We further analyze this phenomenon at the end of this paper.

As mentioned before, the threshold OD is different for the two phases. This is illustrated in Fig. 8, where we repeated the experiment of Fig. 7 for different values of the OD. In this experiment, the OD was varied *at fixed cloud size* by transferring a variable amount of population into the $F = 1$ state, which is not interacting with the pattern-forming laser beam. Indeed, this specific measurement was performed without repumping light in the laser beam. Because of the low saturation ($s = 1.7 \times 10^{-3}$), the atomic population in $F = 2$ remained constant during the 1-ms-long pattern formation sequence. We plot the diffracted energy for both AFM (squares) and GSC (stars) phases versus B_x (note the double logarithmic scale). The open circles correspond to measurements where no structured phase was observed (we set the corresponding E_d to 10^{-3} for display purpose). In Fig. 8, all curves have been scaled such that the growth rate is unity for $B_x = 0 \text{ G}$ (here offset by 0.008 G for better display). For the low laser intensity considered here ($I = 3.6 \text{ mW/cm}^2$), the transition from AFM to GSC occurs around $B_x \approx 50 \text{ mG}$. The point here is to compare the relative behaviors of the GSC and AFM phases as the OD is decreased. As can be seen, the GSC phase decreases faster. A gap between the two phases develops as the OD is decreased, and appears around OD = 57 for this set of parameters. This gap broadens as the OD is further decreased. Eventually, the GSC phase vanishes while the AFM phase is still observed (curve 7, OD = 26). For OD = 18 (not shown in Fig. 8), the AFM phase is no longer observed. This difference in OD thresholds between the two phases is also observed in the numerical simulations.

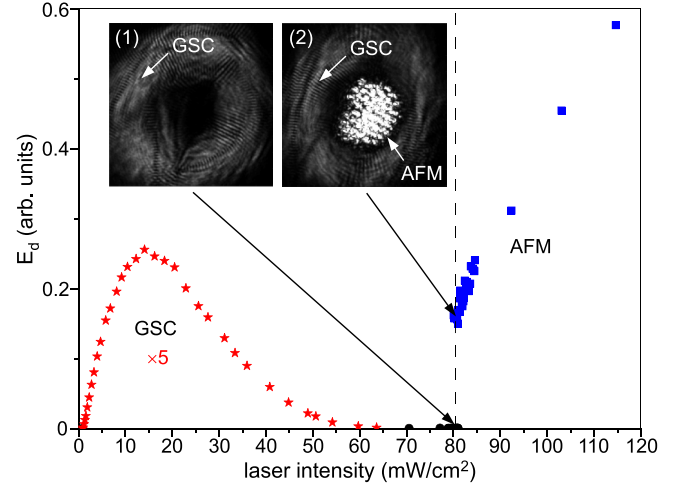


FIG. 9. Transition from GSC to AFM phase via laser intensity tuning (experimental). We plot the diffracted energy E_d at beam center as a function of increasing laser intensity, and we observe the transition from the GSC phase (stars, $\times 5$) to the AFM phase (squares). The circles correspond to $E_d = 0$. The dashed line indicates the approximate position of the intensity threshold for the AFM phase. The insets illustrate the “blinking” behavior of the AFM phase in the bistability region (see text). The magnetic field is $B_x = 0.71 \text{ G}$.

B. Laser-intensity-induced transition

A second way to induce the transition between the GSC and AFM phases is by tuning the laser intensity. We start by setting $B_x \neq 0$, at a value which sustains the GSC phase, and increase the laser intensity. Above a certain critical intensity, the optical pumping rate responsible for the establishment of an orientation will become larger than the substate mixing rate due to the Larmor precession induced by B_x . There, we expect a transition to the AFM phase to occur.

The outcome of such an experiment is depicted in Fig. 9, where we plot the diffracted energy detected in the \perp channel and *at beam center*, as a function of laser intensity. The magnetic field is $B_x = 0.71 \text{ G}$. At low intensity, we first observe the onset of the GSC phase above a threshold intensity of $I_{\text{th}}^{\text{GSC}} \approx 0.9 \text{ mW/cm}^2$. The diffracted energy then increases up to a maximum reached for $I = 15 \text{ mW/cm}^2$. We then observe a *decrease* of E_d , until the GSC phase vanishes at beam center. Although this behavior is also observed in the numerics for certain parameters (see discussion below), we do not have a clear physical interpretation for it at the moment. The GSC phase thus exhibits both lower and upper intensity thresholds. We stress that this behavior is unique among the “magnetic” phases observed in our experiment [17]. It was however observed, unsurprisingly, for the self-organization mechanism based on excited-state population [16].

For a critical intensity of $I_{\text{th}}^{\text{AFM}} \approx 80 \text{ mW/cm}^2$, the AFM phase turns on abruptly. We observe a quite narrow region of bistability around the critical intensity, with large fluctuations of E_d as the AFM phase turns randomly on and off from shot to shot, as illustrated by the NF images in Fig. 9. These images correspond to consecutive single-shot near-field images. It can be seen from image (1) that the GSC phase has vanished from beam center (highest laser intensity), but is still present in the

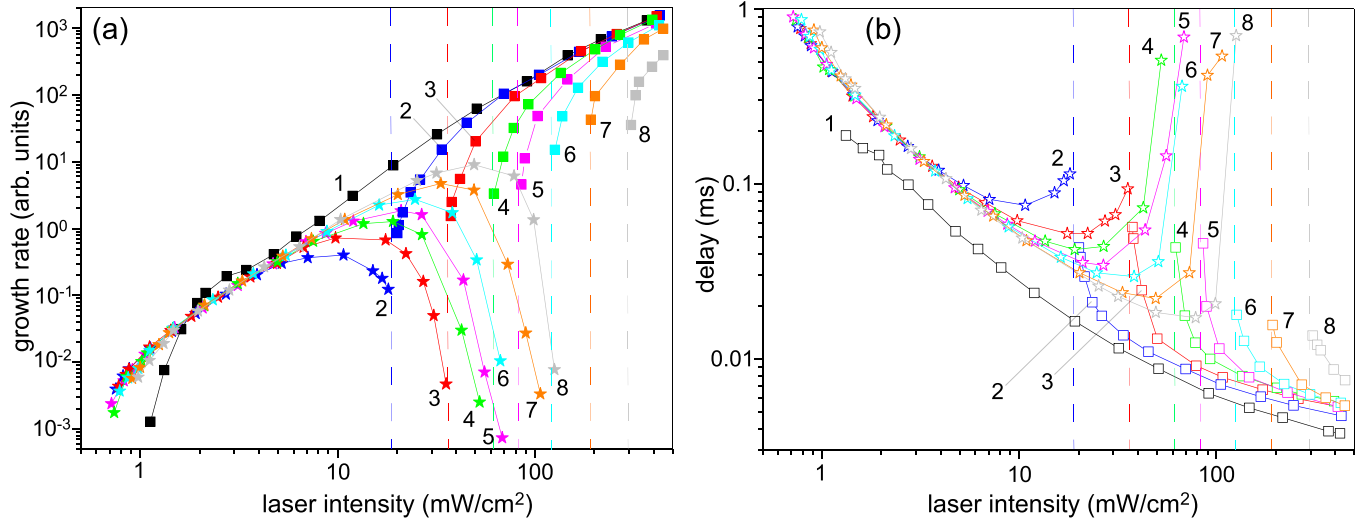


FIG. 10. Behavior of GSC and AFM phases versus laser intensity for different B_x values (experimental). We report (a) the growth rate and (b) the delay for different values of B_x : (1) $B_x = 0$, (2) $B_x = 0.14$ G, (3) $B_x = 0.28$ G, (4) $B_x = 0.5$ G, (5) $B_x = 0.71$ G, (6) $B_x = 1.06$ G, (7) $B_x = 1.56$ G, and (8) $B_x = 2.27$ G. The stars (squares) correspond to the GSC (AFM) phase. The vertical dashed lines indicate the positions of AFM thresholds.

wings. The AFM phase appears first at beam center (2), in the region where the GSC phase is depleted.

The experiment of Fig. 9 was repeated for different B_x values. We show in Fig. 10 how the growth rates and delays behave in the two phases (note the double logarithmic scale). The stars (respectively, squares) correspond to the GSC (respectively, AFM) phase. Concentrating first on the growth rate [Fig. 10(a)], we observe that for the GSC phase it first increases and then decreases with increasing laser intensity, in agreement with Fig. 9. The intensity for which the maximum growth rate is obtained is seen to increase with B_x . On the contrary, we notice that below ≈ 5 mW/cm² all data corresponding to different B_x collapse on the same curve. This suggests that the lower intensity threshold for the GSC phase is nearly independent of B_x (this was confirmed by direct measurements). Looking now at the growth rate for the AFM phase, we observe above threshold an increase with laser intensity toward a common curve seemingly independent of B_x at high intensities. The AFM threshold intensity is observed to increase linearly with B_x , with a slope of 127 mW cm⁻² G⁻¹. The linear dependence of the AFM threshold intensity with B_x is consistent with the picture that, for this orientation-based phase, light-induced Zeeman pumping needs to overcome the level mixing associated with the transverse magnetic field. As B_x is increased, the “gap” between the GSC and AFM phases widens, and the magnitude of the discontinuity at the AFM threshold increases.

We now turn to Fig. 10(b) showing the behavior of the delay. For the GSC phase, we observe a divergence of τ_d near both lower and upper intensity thresholds. As mentioned before, the lower threshold is nearly B_x independent, whilst the upper one does strongly depend on B_x . For the AFM phase, the delay is seen to diverge at threshold and then monotonously decreases as the laser intensity is increased.

Our numerical simulations reproduce qualitatively most of the experimental observations. For instance, Figure 11(a) shows the intensity-induced transition between GSC and

AFM phases for different B_x values, to be compared with Figs. 9 and 10. We recover the results that the GSC intensity threshold is nearly independent on B_x , while the AFM intensity threshold increases linearly with B_x . Note, however, the rather large quantitative mismatch in the values of, e.g., I_{th}^{AFM} , which are smaller in the simulations. We attribute this difference to the ground-state structure of ⁸⁷Rb, which is more complex than a spin-1 system.

We also observe a qualitative difference with the experiment, which is that we cannot reproduce the full behavior seen in Fig. 9 with a single set of simulation parameters. Using the values of experimental parameters of Fig. 10 yields the curves in Fig. 11(a), with the abrupt switching of the AFM phase but no vanishing of the GSC phase at large intensity. Using different parameters (lower OD) yields the vanishing of the GSC at large intensity but a continuous switching of the AFM. The origin of this discrepancy remains unexplained at the moment.

Finally, Fig. 11(b) shows a simulated NF image obtained using an incident Gaussian beam, just above the AFM threshold: the AFM phase is seen to appear at the beam’s center, while the GSC phase is present in the wings, in close connection with what is observed experimentally [image (2) in Fig. 9].

C. Nature of the different transitions

As can be readily seen from Figs. 9 and 10, several types of bifurcations can be observed in this system. For all B_x values, the GSC phase exhibits a smooth, continuous evolution of the diffracted intensity as its lower intensity threshold is crossed, which indicates a second-order transition. The same is observed for the AFM phase in the particular case of $B_x = 0$. However, when $B_x \neq 0$, the transition to AFM becomes clearly first order, with a discontinuity of E_d at threshold whose magnitude increases with B_x . These behaviors are confirmed by the numerics [Fig. 11(a)].

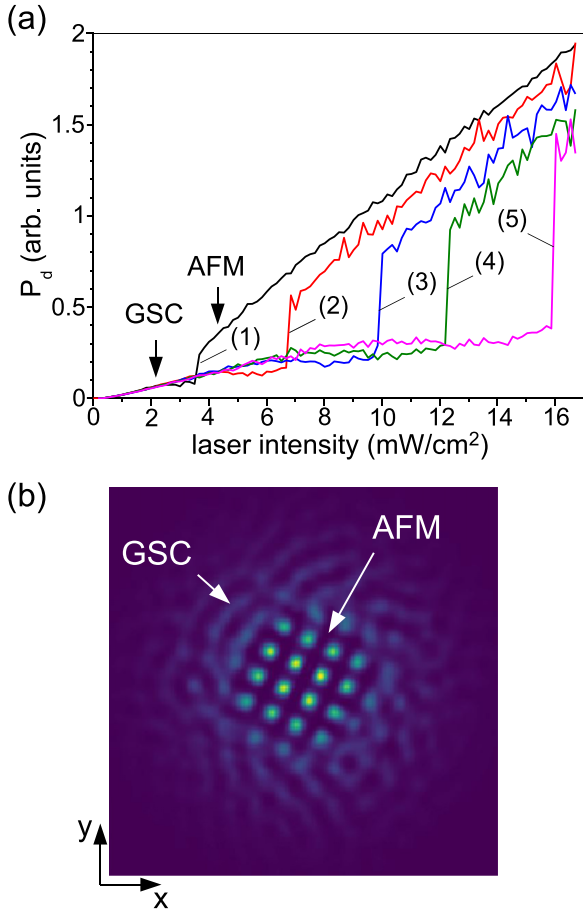


FIG. 11. Transition from GSC to AFM phase via laser intensity tuning (numerical). (a) Steady-state diffracted power P_d as a function of laser intensity for different B_x values: (1) $B_x = 0.2$ G, (2) $B_x = 0.4$ G, (3) $B_x = 0.6$ G, (4) $B_x = 0.76$ G, and (5) $B_x = 1$ G. (b) NF image just above the AFM threshold (simulation with Gaussian beam), showing the coexistence of AFM (center) and GSC (wings).

One may use the phenomenon of critical slowing down to characterize the nature of the bifurcation. In the critical regime, the delay is expected to scale as a power law with distance to threshold: $\tau_d \propto (I - I_{th})^{-\alpha}$. The value of the critical exponent α can be used as a smoking gun for different types of bifurcations [33]. However, the determination of α can be delicate in our case, as illustrated in Fig. 12(a). We plot in log-log scale the delay for the GSC phase at $B_x = 0.71$ G as a function of the intensity distance to threshold $I - I_{th}^{GSC}$. The threshold value $I_{th}^{GSC} = 0.9$ mW/cm² is obtained by linear extrapolation of the measured $E_d(I)$ data to $E_d = 0$. This yields the stars in Fig. 12(a). As can be seen, the data deviate from a power law at low $I - I_{th}^{GSC}$ values and exhibit a curvature which is consistent with an overestimation of I_{th}^{GSC} . Indeed, if we use a “rescaled” threshold intensity equal to $0.5 \times I_{th}^{GSC}$, we obtain the circles which nicely fit a power law with $\alpha = 0.86$ (solid line). Several reasons can lead to this overestimation of the threshold intensity. First, the sensitivity of our time-resolved detection is somewhat limited. Second, the measured $E_d(I)$ curve is smooth, and thus the linear extrapolation yields a threshold value larger than the actual one. Finally, close to

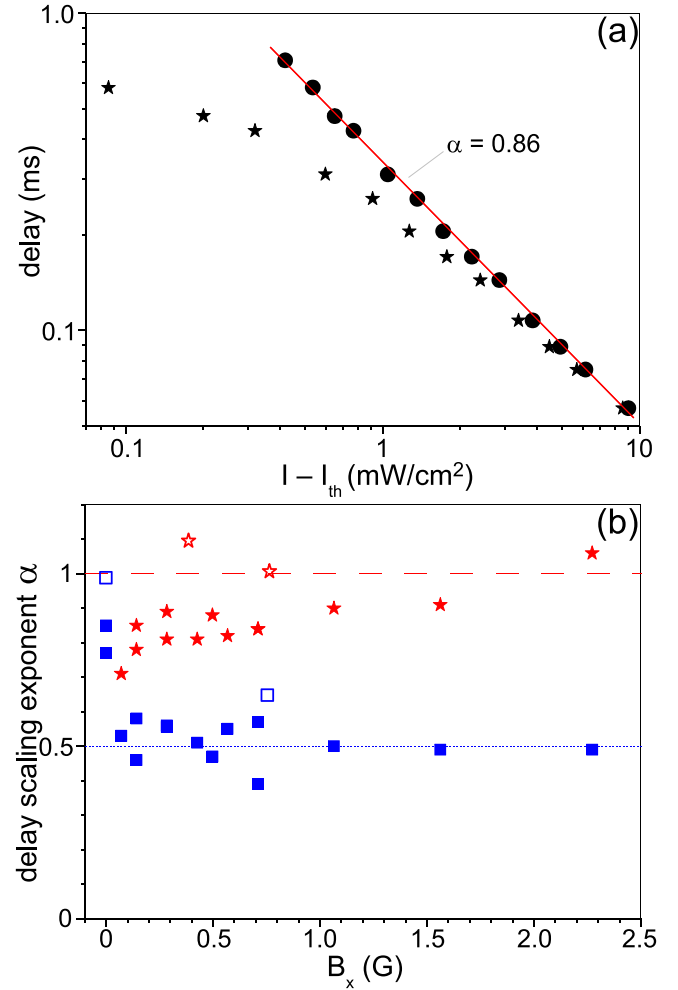


FIG. 12. Critical slowing down and scaling exponents. (a) GSC delay for $B_x = 0.71$ G plotted versus distance from threshold $I - I_{th}$ (experimental). Note the double logarithmic scale. The stars and circles respectively correspond to the measured and rescaled threshold intensity (see text). (b) Scaling exponent for the GSC phase (stars) and the AFM phase (squares) versus B_x . The solid and open symbols correspond to experimental and numerical data, respectively. The dashed and dotted lines show theoretically expected values for the two types of bifurcations (see text).

threshold the delay diverges and may become larger than the laser pulse duration (1 ms). In this situation, one measures $E_d = 0$ even though the threshold is not yet reached.

Figure 12(b) shows a summary of the values of α experimentally obtained for different B_x , for both GSC (solid stars) and AFM (solid squares) phases. The data are those of Fig. 10. The open symbols correspond to the numerical results. The solid and dashed lines correspond to the theoretical expectations for second-order ($\alpha = 1$) and first-order ($\alpha = 0.5$) transitions. Despite the relatively large uncertainty on experimental values of α due to the difficulty in determining I_{th} , we observe the following behaviors. For the GSC phase, in the whole B_x range where it is observed, the exponent is close to 1 and consistent with a pitchfork bifurcation [33,34], which is continuous (second-order). The same is true for the AFM phase close to $B_x = 0$, that is where it appears in a primary

transition from an homogeneous state and not in a secondary transition after the GSC phase as in Fig. 9. In the latter case, we find an exponent close to 0.5 as expected for a first-order transition. These observations are confirmed by the numerics.

VI. CONCLUSION

In this paper we have explored some aspects of magnetic self-organization in a cold atomic cloud due to the coupling with a retroreflected laser beam. We investigated the properties of an original phase based on the spontaneous spatial modulation of the $\Delta m = 2$ ground-state coherence. The richness of this system allowed us to study the transition between phases of different nature and the competition between different self-organization mechanisms. Further investigations are required to gain a better understanding of the nature of the GSC phase and, in particular, of the interplay between orientation and ground-state coherence. A possible experimental development toward achieving this goal would be to use a spatial light modulator to seed the desired dipolar or quadrupolar terms by a spatial modulation of either the input beam's direction of polarization or its helicity.

Future developments could include the study of the observed bifurcations using the statistics of topological defects, in the framework of the Kibble-Zurek mechanism [35]. The search for optically controllable, localized magnetic structures [36] of various natures is also an exciting perspective. The bistability region at the first-order bifurcation to the AFM phase for $B_x \neq 0$ seems a promising candidate to observe such effects. Also, the diffractive coupling scheme offers the possibility to tailor the nature (and not only the magnitude) of the interactions between atoms, by modifying either the polarization or the spatial intensity distribution of the light fed back to the atoms, which could lead to the observation of new phases [17] and interesting phenomena such as, e.g., frustration.

ACKNOWLEDGMENTS

We thank G.-L. Oppo for useful discussions. The collaboration between the two groups is supported by the CNRS-funded Laboratoire International Associé (LIA) "Solace", the European Training Network ColOpt (funded by the European Union Horizon 2020 programme under the Marie Skłodowska-Curie action, Grant No. 721465), and the Global Engagement Fund of the University of Strathclyde.

-
- [1] I. Bloch, J. Dalibard, and S. Nascimbène, Quantum simulations with ultracold quantum gases, *Nat. Phys.* **8**, 267 (2012).
 - [2] C. Gross and I. Bloch, Quantum simulations with ultracold atoms in optical lattices, *Science* **357**, 995 (2017).
 - [3] J. Struck *et al.*, Quantum simulation of frustrated classical magnetism in triangular optical lattices, *Science* **333**, 996 (2012).
 - [4] D. Greif, T. Uehlinger, G. Jotzu, L. Tarruel, and T. Esslinger, Short-range quantum magnetism of ultracold fermions in an optical lattice, *Science* **340**, 1307 (2013).
 - [5] A. Mazurenko, C. S. Chiu, G. Ji, M. F. Parsons, M. Kanász-Nagy, R. Schmidt, F. Grusdt, E. Demler, D. Greif, and M. Greiner, A cold-atom Fermi-Hubbard antiferromagnet, *Nature (London)* **545**, 462 (2017).
 - [6] H. Labuhn, D. Barredo, S. Ravets, S. de Léséleuc, T. Macrì, T. Lahaye, and A. Browaeys, Tunable two-dimensional arrays of single Rydberg atoms for realizing quantum Ising models, *Nature (London)* **534**, 667 (2016).
 - [7] J. Stuhler, A. Griesmaier, T. Koch, M. Fattori, T. Pfau, S. Giovanazzi, P. Pedri, and L. Santos, Observation of Dipole-Dipole Interaction in a Degenerate Quantum Gas, *Phys. Rev. Lett.* **95**, 150406 (2005).
 - [8] H. Kadau, M. Schmitt, M. Wenzel, C. Wink, T. Maier, I. Ferrier-Barbut, and T. Pfau, Observing the Rosensweig instability of a quantum ferrofluid, *Nature (London)* **530**, 194 (2016).
 - [9] A. V. Gorshkov, S. R. Manmana, G. Chen, J. Ye, E. Demler, M. D. Lukin, and A. M. Rey, Tunable Superfluidity and Quantum Magnetism with Ultracold Polar Molecules, *Phys. Rev. Lett.* **107**, 115301 (2011).
 - [10] S. A. Moses, J. P. Covey, M. T. Miecnikowski, B. Yan, B. Gadway, J. Ye, and D. S. Jin, Creation of a low-entropy quantum gas of polar molecules in an optical lattice, *Science* **350**, 659 (2015).
 - [11] H. Bernien, S. Schwartz, A. Keesling, H. Levine, A. Omran, H. Pichler, S. Choi, A. S. Zibrov, M. Endres, M. Greiner, V. Vuletić, and M. D. Lukin, Probing many-body dynamics on a 51-atom quantum simulator, *Nature (London)* **551**, 579 (2017).
 - [12] J. Zeiher, J.-Y. Choi, A. Rubio-Abadal, T. Pohl, R. van Bijnen, I. Bloch, and C. Gross, Coherent Many-Body Spin Dynamics in a Long-Range Interacting Ising Chain, *Phys. Rev. X* **7**, 041063 (2017).
 - [13] J. A. Greenberg, B. L. Schmittberger, and D. J. Gauthier, Bunching-induced optical nonlinearity and instability in cold atoms, *Opt. Express* **19**, 22535 (2011).
 - [14] G. Labeyrie, E. Tesio, P. M. Gomes, G.-L. Oppo, W. J. Firth, G. R. M. Robb, A. S. Arnold, R. Kaiser, and T. Ackemann, Optomechanical self-structuring in a cold atomic gas, *Nat. Photonics* **8**, 321 (2014).
 - [15] B. L. Schmittberger and D. J. Gauthier, Transverse optical and atomic pattern formation, *J. Opt. Soc. Am. B* **33**, 1543 (2016).
 - [16] A. Camara, R. Kaiser, G. Labeyrie, W. J. Firth, G.-L. Oppo, G. R. M. Robb, A. S. Arnold, and T. Ackemann, Optical pattern formation with a two-level nonlinearity, *Phys. Rev. A* **92**, 013820 (2015).
 - [17] G. Labeyrie, I. Kresic, G. R. M. Robb, G.-L. Oppo, R. Kaiser, and T. Ackemann, Magnetic phase diagram of light-mediated spin structuring in cold atoms, *Optica* **5**, 1322 (2018).
 - [18] I. Kresic, G. Labeyrie, G. R. M. Robb, G.-L. Oppo, P. M. Gomes, P. Griffin, R. Kaiser, and T. Ackemann, Spontaneous light-mediated magnetism in cold atoms, *Commun. Phys.* **1**, 33 (2018).
 - [19] P. Domokos and H. Ritsch, Collective Cooling and Self-Organization of Atoms in a Cavity, *Phys. Rev. Lett.* **89**, 253003 (2002).

- [20] K. Baumann, C. Guerlin, F. Brennecke, and T. Esslinger, Dicke quantum phase transition with a superfluid gas in an optical cavity, *Nature (London)* **464**, 1301 (2010).
- [21] J. Léonard, A. Morales, P. Zupancic, T. Esslinger, and T. Donner, Supersolid formation in a quantum gas breaking a continuous translational symmetry, *Nature (London)* **543**, 87 (2017).
- [22] M. A. Neto and J. R. de Souza, Transverse Ising antiferromagnetic in a longitudinal magnetic field: Study of the ground state, *Phys. Lett. A* **330**, 322 (2004).
- [23] M. A. Neto and J. R. de Souza, Phase diagrams of the transverse Ising antiferromagnet in the presence of the longitudinal magnetic field, *Phys. A* **392**, 1 (2013).
- [24] T. Ackemann and W. Lange, Non- and nearly hexagonal patterns in sodium vapor generated by single-mirror feedback, *Phys. Rev. A* **50**, R4468(R) (1994).
- [25] A. Aumann, E. Büthe, Y. A. Logvin, T. Ackemann, and W. Lange, Polarized patterns in sodium vapor with single mirror feedback, *Phys. Rev. A* **56**, R1709(R) (1997).
- [26] I. Kresic, G. R. M. Robb, G. Labeyrie, R. Kaiser, and T. Ackemann, Inversion symmetry breaking in spin patterns by a weak magnetic field, *Phys. Rev. A* **99**, 053851 (2019).
- [27] M. Auzinsh, D. Budker, and S. Rochester, *Optically Polarized Atoms: Understanding Light-Atom Interactions* (Oxford University, Oxford, England, 2010).
- [28] W. J. Firth, Spatial instabilities in a Kerr medium with single feedback mirror, *J. Mod. Opt.* **37**, 151 (1990).
- [29] T. Ackemann, G. Labeyrie, G. Baio, I. Kresic, J. G. M. Walker, A. C. Boquete, P. Griffin, W. J. Firth, R. Kaiser, G.-L. Oppo, and G. R. M. Robb, Self-organization in cold atoms mediated by diffractive coupling, *Atoms* **9**, 35 (2021).
- [30] G. Grynberg, A. Maître, and A. Petrossian, Flowerlike Patterns Generated by a Laser Beam Transmitted through a Rubidium Cell with Single Feedback Mirror, *Phys. Rev. Lett.* **72**, 2379 (1994).
- [31] J. A. Greenberg and D. J. Gauthier, Steady-state, cavityless, multimode superradiance in a cold vapor, *Phys. Rev. A* **86**, 013823 (2012); High-order optical nonlinearity at low light levels, *Europhys. Lett.* **98**, 24001 (2012).
- [32] J. R. Treddice, G. L. Lippi, P. Mandel, B. Charasse, A. Chevalier and B. Picqu , Critical slowing down at a bifurcation, *Am. J. Phys.* **72**, 799 (2004).
- [33] E. D. Leonel, Defining universality classes for three different local bifurcations, *Commun. Nonlinear Sci. Numer. Simul.* **39**, 520 (2016).
- [34] S. H. Strogatz, *Nonlinear Dynamics and Chaos: With Applications to Physics, Biology, Chemistry and Engineering* (Perseus, Cambridge, MA, 2001).
- [35] G. Labeyrie and R. Kaiser, Kibble-Zurek Mechanism in the Self-Organization of a Cold Atomic Cloud, *Phys. Rev. Lett.* **117**, 275701 (2016).
- [36] B. Sch pers, M. Feldmann, T. Ackemann, and W. Lange, Interaction of Localized Structures in an Optical Pattern-Forming System, *Phys. Rev. Lett.* **85**, 748 (2000).